

Water dynamics inside a cathode channel of a polymer electrolyte membrane fuel cell

Mamdud Hossain*, Sheikh Zahidul Islam, Amy Colley-Davies, Ebenezer Adom

School of Engineering, Robert Gordon University, Schoolhill, Aberdeen AB10 1FR, UK

ARTICLE INFO

Article history:

Received 16 March 2012

Accepted 13 August 2012

Available online 12 September 2012

Keywords:

Water dynamics
Surface coverage
Cathode channel
Gas diffusion layer
Volume of fluid
Surface wettability

ABSTRACT

The present study focuses on the investigation of water dynamics inside a polymer electrolyte membrane fuel cell using two different modelling approaches: Eulerian two-phase mixture and volume of fluid interface tracking models. The Eulerian two-phase mixture model has provided overall information of species distribution inside a fuel cell and identified that the liquid water usually accumulates under the land area. The volume of fluid interface tracking model has then been implemented to investigate the emergence of water droplets from the gas diffusion layer into the cathode channel and the subsequent removal of water from the channel. Further, the effects of the location of water emergence in the cathode channel on the dynamic behavior of liquid water have been investigated. The present study shows that the water emerging into the channel near the side walls greatly reduces the surface water coverage of the channel. In order to control the water path into the channel near side walls, a further discussion has been provided that a gas diffusion layer design based on hydrophilic fibres distributed inside a hydrophobic fibre matrix could provide a precisely controlled water path through the gas diffusion layer.

© 2012 Elsevier Ltd. All rights reserved.

1. Introduction

A polymer electrolyte membrane (PEM) fuel cell, which has been considered to be a suitable candidate for solving future energy crisis, converts chemical energy into electricity in a cleaner fashion. PEM fuel cells can be employed in many applications including automobiles, combined heat and power unit, stationary and portable power system [1]. Despite having many attractive benefits, the widespread deployment of PEM fuel cell has been hampered by high cost and durability. The high cost of a PEM fuel cell stems from using expensive platinum as catalyst to maintain electrochemical reaction. Much research has been directed to reduce platinum uses [2,3]. Another way to reduce the cost would be to increase the performance of existing design. In this respect, water management is a critical issue in enhancing the PEM fuel cell performance.

A PEM fuel cell operates by combining oxygen and hydrogen and producing water as a byproduct. Moreover, water is also needed to keep the electrolyte membrane hydrated. This is done by hydrating both air and fuel streams. As a result, the cathode gas diffusion layer contains a large amount of water, which eventually flows into the cathode channel and is then carried away with the airstream [4]. In order to improve the performance, the water from the cathode

channel should be removed quickly and the water coverage on the gas diffusion layer (GDL) surface should be small. This would allow more oxygen to diffuse through the gas diffusion layer to the reaction sites. A thorough understanding of the process of water removal through the cathode channel is required in order to devise a good water management strategy or to develop a new architecture of a PEM fuel cell.

Because of the importance of water management, several studies have been reported that deals with the problem of water management through numerical modelling study by developing of two-phase models that takes into account phase changes in water vapour and liquid water, multi-component species transport and electrochemistry. Natarajan and Nguyen [5] employed a pseudo three-dimensional model to investigate liquid water movement inside the cathode electrode. In the work of Wang et al. [6], and You and Liu [7] both liquid and vapour phase of water flows have been considered, but only inside the cathode gas diffusion layer. In a follow-up paper, You and Liu [8] reported a two-dimensional, two-phase coupled PEM model, which showed that the liquid water also influenced the oxygen transport. Berning and Djilali [9] also developed a three-dimensional, multi-phase, multi-component model considering heat and mass transfer. In their study liquid water transport inside the GDL was numerically modelled by using viscous and capillary effects. This method was also implemented by Mazumder and Cole [10]. Min [11] developed a three-dimensional, two-phase, non-isothermal model based on

* Corresponding author. Tel.: +44 (0) 1224262351; fax: +44 (0) 1224262444.
E-mail address: M.Hossain@rgu.ac.uk (M. Hossain).

two-fluid model. Meng [12] developed a mixed domain two-fluid PEM fuel cell model, where water transport through the membrane was calculated by solving a conservation equation for the water content in the membrane. Further details in two-phase modelling of PEM fuel cell can be found in the recent review paper by Khan et al. [13].

Though all the two-phase modelling studies mentioned above provided significant contribution to knowledge, these models were unable to predict the dynamic behavior of the emergence of liquid water as droplet, and subsequent droplet growth, coalescing and the formation of slug or water film in the channel. Several papers have appeared recently in literature concerning the dynamic behavior of water droplet movement through the cathode channel [14–26]. Experimental studies have provided visual description of water droplet egress from the GDL and subsequent slug formation in the channel [4,23,24]. However, because of the use of transparent wall for visual access, the experimental technique cannot reproduce the key role played by channel walls in water removal [19]. In this respect, the application of the volume of fluid (VOF) method in the computational fluid dynamics framework has provided many insights into the water dynamics in the cathode channel [14–22]. Cai et al. [14] investigated the effects of surface wettability of GDL on movement of a single droplet and film and concluded that a combination of the hydrophobic GDL with hydrophilic side walls was beneficial for water removal. Zhan et al. [15] also investigated the droplet and film movements through a serpentine channel and provided similar conclusion to Cai et al. [14]. Jiao and Zhou [16] were focused on developing an innovative gas diffusion layer with microchannel linking the catalyst layer with the flow channel. Quan et al. [17] investigated the water dynamics inside a serpentine channel with various initial conditions of water presence in the channel. In a series of papers, Zhu et al. [18–20] investigated the process of water droplet emergence, growth, deformation and detachment. Zhu et al. [18] investigated the dynamics of a single water droplet in the cathode channel by implementing a VOF model. The simulation was carried out on a two-dimensional geometry which was not a realistic presentation of the actual physics. In subsequent papers, Zhu et al. [19,20] modified the computational domain to a three-dimensional geometry. The detail description of water droplet emergence, growth, deformation and detachment of a single droplet has been provided through a parametric study of the effects of surface wettability, air flow velocity, water injection velocity and the size of the pore. Ding et al. [21,22] have provided a more realistic representation of water droplet interaction by setting up water emergence into the channel through a number of pores. Their study shows that water droplets after emerging from pores, merge into larger slugs and then accumulate on the side walls before being driven out of the channel.

Based on the above literature review, it is clear that the water dynamics in a fuel cell has to be understood at multi-levels using models that include the entire detailed physics e.g. multi-phase interface tracking between gas-phase and liquid water-phase, multi-components, mass transfer, electrochemical reaction and water-phase change effects. In the present study, two different modelling approaches have been implemented to provide complete information of water dynamics in a fuel cell. The first modelling approach is based on the Eulerian two-phase concept, which takes into account all parts of PEMFC including the membrane, catalyst layers, GDLs and gas flow channels. In the second modelling approach, the interface of the liquid water and air phase has been tracked through a cathode flow channel by a VOF model.

Water generated in the catalyst layer diffuses through the gas diffusion layer into the flow channel. A GDL is made of randomly distributed fibres and as such water flows through the random flow paths inside the GDL into the channel and it is very difficult to

predict which flow path water would take into the channel. In reality, experimental studies [23–26] show that water enters the channel from the GDL preferentially through certain pores and the distance between the pore is quite large. In previous studies, the emergence of water into the channel from the GDL has been modelled by a single pore (inlet) [18–20], multiple pores but very closely packed to each other [21] and two pores across the width [22]. Obviously, the size and the distance between the water emerging pores would have major effects on the surface coverage of a GDL and the water fraction inside the flow channel. The present study seeks to provide a systematic study of water droplet dynamics for different pore distances and pore sizes. The main objective of this study is to identify an optimum pore arrangement that would provide minimum water coverage on the GDL surface.

2. Mathematical model

The numerical simulation procedure in the present study is based on two different modelling approaches. In the first modelling approach, a Eulerian two-phase mixture model, that includes the transport of hydrogen, oxygen, water vapour and liquid water through the flow channels, the GDL, the catalyst layers, the membrane, and the electrochemical reactions and the phase change effects, has been developed. This modelling approach provides information regarding PEM fuel cell performance characteristics and species distribution inside the cell as average values. This method does not provide the crucial information regarding the dynamics of liquid water emergence, growth, coalescence and movement in the channel. Therefore, a second modelling approach based on the multi-phase volume of fluid (VOF) interface tracking between the air and liquid water-phase has been employed to provide further insight into the liquid water transport inside the flow channel and to develop an effective water removal technique.

2.1. Governing equations for the Eulerian two-phase mixture model

The governing equations for the PEM fuel cell model consist of continuity, momentum and species transport equations. These equations represent the transport phenomenon inside the catalyst layers, gas diffusion layers and the flow channels. To represent the electrochemistry and the transport phenomena through the membrane, appropriate source terms are applied at the anode and cathode catalyst layers.

2.1.1. The mass conservation equation (continuity equation)

$$\nabla(\rho \vec{u}) = 0 \quad (1)$$

where ρ is the fluid density and \vec{u} is the velocity vector.

2.1.2. The momentum conservation equation

$$\nabla(\rho \vec{u} \vec{u}) = -\nabla P + \nabla \mu \nabla(\vec{u}) + S_u \quad (2)$$

where P is the pressure and S_u is the source term.

In the flow channel, S_u is zero. In the gas diffusion layers and the catalyst layers Darcy's law term is added to the momentum equations to represent the momentum related to the porous media. This source term is expressed as:

$$S_u = -\frac{\mu \vec{u}}{K} \quad (3)$$

where, K is permeability of the porous media (gas diffusion layers and catalyst layers).

2.1.3. The species conservation equation

$$\nabla(\rho \vec{u} X_k) = \nabla(D_k^{eff} \rho \nabla X_k) + S_k \quad (4)$$

where index k refers to oxygen, hydrogen, water vapour and liquid water. X_k is the molar concentration of species k and D_k^{eff} is the effective diffusion coefficient of species k .

The source terms S_k in the species conservation Eq. (4) are defined as zero for all regions of the model except at the catalyst layers. Species source term for anode and cathode catalyst layers are expressed as below.

Consumption of hydrogen due to electrochemical effects at the anode catalyst layer

$$S_{H_2} = -\frac{IA}{2F} M_{H_2} \quad (5)$$

Consumption of oxygen due to electrochemical effects at the cathode catalyst layer

$$S_{O_2} = -\frac{IA}{4F} M_{O_2} \quad (6)$$

Production of water and the flux of water due to electrochemical effects at the cathode catalyst layer

$$S_{cw} = \frac{[1 + 2\alpha]IA}{2F} M_{H_2O} \quad (7)$$

The flux of water due to electrochemical effects at the anode catalyst layer

$$S_{aw} = -\frac{\alpha IA}{F} M_{H_2O} \quad (8)$$

where, A is the area of the catalyst layer. The current density I and net water transfer coefficient α are used to determine these source terms.

To account for phase changes between water vapour and liquid water, the following source term has been added in the species transport equation for liquid water and water vapour (4) according to [27]

$$S_{wlp} = -S_{wvp} = \frac{(P_{wv} - P_{wv}^{sat})}{RT} \times M_{H_2O} \times k_c \quad (9)$$

where k_c is the water vapour condensation rate.

The diffusion coefficient of species can be expressed as [11]:

$$D_k = D_{k,ref} \left(\frac{T}{T_{ref}} \right)^{\frac{3}{2}} \left(\frac{P_{ref}}{P} \right) \quad (10)$$

where, $D_{k,ref}$ is the reference value at T_{ref} and P_{ref} . The diffusivity values obtained from Eq. (10) needs to be corrected for porous regions.

The diffusion coefficient in the porous regions can be expressed as

$$D_k^{eff} = f(\epsilon)g(s)D_k \quad (11)$$

Tomadakis and Sotirchos model has been shown to provide the best representation of effective diffusivity and this percolation theory based diffusion model for random fibrous porous medium is given by [28]

$$f(\epsilon) = \epsilon \left(\frac{\epsilon - \epsilon_p}{1 - \epsilon_p} \right)^\alpha \quad (12)$$

where ϵ_p is the percolation threshold and equal to 0.11. α is the empirical constant which depends on the direction. α is 0.521 and 0.785, for in-plane and through-plane diffusion, respectively.

The effects of saturation on the effective diffusivity of species can be generally given by power law model according to [28],

$$g(s) = (1 - s)^2 \quad (13)$$

A number of auxiliary equations need to be solved to model the electrochemical reactions and determine the local current density and net water transfer coefficient. The auxiliary equations are based on the assumption of using Nafion 117 membrane, and are taken from the work of Springer et al. [29].

2.2. Auxiliary equations

The auxiliary model equations, needed to be solved to determine the net water transfer coefficient and cell voltage at an average current density, are summarised below.

2.2.1. Water transport in the membrane

When electrochemical reaction takes place inside a fuel cell, water molecules are dragged through the membrane from the anode to the cathode with protons. This is known as electro-osmotic drag. In addition, some of the water produced at the cathode transports through the membrane from the cathode side to the anode side due to concentration gradient, known as back-diffusion. Hence, the amount of water transported across the membrane is equal to the difference in water transported by the back-diffusion and that by electro-osmotic drag [30].

In order to reduce complexity in the model development, it is assumed that the water transport across the membrane is one-dimensional and can be approximated by a single step linear difference in concentrations at the cathode and anode side. The final expression for the net water transfer coefficient per proton is [30]:

$$\alpha = n_d - \frac{FD_{H_2O}[C_{H_2O_c} - C_{H_2O_a}]}{It_m} \quad (14)$$

where D_{H_2O} represents water diffusion coefficient, $C_{H_2O_a}$ and $C_{H_2O_c}$ represent the molar concentration of water at the anode and cathode side respectively, I is the average current density and t_m is the membrane thickness and F is the Faraday's constant.

Electro-osmotic drag coefficient describes the amount of water dragged by each proton across the membrane from the anode to the cathode side and expressed as [30],

$$\begin{aligned} n_d &= 0.0049 + 2.02a_a - 4.53a_a^2 + 4.09a_a^3; \quad a_a \leq 1 \\ n_d &= 1.59 + 0.159(a_a - 1); \quad a_a > 1 \end{aligned} \quad (15)$$

where, water activity is defined as [30],

$$a_k = \frac{X_{H_2O,k}P}{D_{H_2O,k}^{sat}} \quad (16)$$

where P is the cell pressure and $X_{H_2O,k}$ is the mole fraction of water on either the anode or cathode side.

Water diffusion coefficient is expressed as [30],

$$D_{H_2O} = 5.5e^{-11}n_d \exp \left[2416 \left(\frac{1}{303} - \frac{1}{T} \right) \right] \quad (17)$$

Water vapour saturation pressure [30]

$$p_{\text{H}_2\text{O}}^{\text{sat}} = \left[0.000644367 + 0.000213948(T-273) \right. \\ \left. + 3.4329e^{-5}(T-273)^2 - 2.70381e^{-7}(T-273)^3 \right. \\ \left. + 8.77696e^{-9}(T-273)^4 \right] - 3.14035e^{-13}(T-273)^5 \\ \left. + 3.82148e^{-14}(T-273)^6 \right] 1.013e^5 \quad (18)$$

Water concentration on the anode and cathode side [30],

$$C_{\text{H}_2\text{O},K} = \frac{\rho_{m,\text{dry}}}{M_{m,\text{dry}}} (0.043 + 17.8a_k - 39.8a_k^2 + 36.0a_k^3); \quad a_k \leq 1 \\ C_{\text{H}_2\text{O},K} = \frac{\rho_{m,\text{dry}}}{M_{m,\text{dry}}} (14 + 1.4(a_k - 1)); \quad a_k > 1 \quad (19)$$

2.2.2. Polarization characteristics

When electrical energy is drawn from the cell, the cell experiences various losses (polarization, overpotential and overvoltage losses) and a result the cell potential drops. The cell voltage can be expressed by the following equation [11]:

$$V_{\text{cell}} = E - \eta_{\text{act}} - \eta_{\text{ohm}} - \eta_{\text{conc}} \quad (20)$$

where E is the equilibrium thermodynamic potential which is calculated using the Nernst equation [11]:

$$E = 1.23 - 0.9 \times 10^{-3}(T - 298) + 2.3 \frac{RT}{4F} \log(p_{\text{H}_2}^2 p_{\text{O}_2}) \quad (21)$$

η_{act} is the activation overpotential, η_{ohm} is the ohmic overpotential and η_{conc} is the concentration overpotential.

Activation overpotential (η_{act}):

The activation overpotential is a function of local current density, exchange current density and concentration of oxygen. The activation overpotential is expressed by Butler–Volmer equation [11],

$$i_a = i_{a,\text{ref}} \left(\frac{C_h}{C_{h,\text{ref}}} \right)^{\frac{1}{2}} \left\{ \exp \left[\frac{\alpha_a \eta_a F}{RT} \eta_{\text{act},a} \right] - \exp \left[-\frac{(1-\alpha_a) \eta_a F}{RT} \eta_{\text{act},a} \right] \right\} \\ i_c = i_{c,\text{ref}} \left(\frac{C_o}{C_{o,\text{ref}}} \right)^{\frac{1}{2}} \left\{ \exp \left[\frac{\alpha_c \eta_c F}{RT} \eta_{\text{act},c} \right] - \exp \left[-\frac{(1-\alpha_c) \eta_c F}{RT} \eta_{\text{act},c} \right] \right\} \quad (22)$$

where $i_{a,\text{ref}}$ and $i_{c,\text{ref}}$ are the exchange current density multiplied by specific area, n is electron number of reaction at anode or cathode and α is the transfer coefficient.

Ohmic overpotential (η_{ohm}):

The ohmic overpotential occurs due to the resistance to electron and ion transfer and can be expressed as [11]:

$$\eta_{\text{ohm}} = \eta_{\text{ohm}}^{\text{el}} + \eta_{\text{ohm}}^{\text{pro}} = I(R^{\text{el}} + R^{\text{pro}}) \quad (23)$$

where R^{el} is the resistance to electron transfer and R^{pro} is the resistance to proton transfer. In general, the resistance to electron transfer is difficult to predict and to avoid complexity in the present model. $R^{\text{el}} = 0.1 \Omega \text{ cm}^2$ is assumed according to the work of Min [11]. The resistance to ion transfer, R^{pro} is calculated using following expression [11]:

$$R^{\text{pro}} = \frac{t_m}{k_m} \quad (24)$$

where, t_m is the height of the membrane and k_m is the phase conductivity of the membrane. The membrane phase conductivity

depends on the temperature and water concentration at anode side and expressed as

$$k_m = 100 \left[0.00514 \left(\frac{M_{m,\text{dry}}}{\rho_{m,\text{dry}}} \right) C_{\text{H}_2\text{O}_a} - 0.00326 \right] \\ \times \exp \left[1268 \left(\frac{1}{303} - \frac{1}{T} \right) \right] \quad (25)$$

Concentration overpotential (η_{conc}):

At high current densities, polarization losses are dominated by concentration overpotential which is caused by slow diffusion of gas through the porous regions. These losses can be determined by, [11]:

$$\eta_{\text{conc}} = -\frac{RT}{nF} \ln \left(1 - \frac{1}{I_L} \right) \quad (26)$$

where I_L is the limiting current density [11]:

$$i_L = \frac{nFD_h C_{k,o}}{H_d} \quad (27)$$

where, D_h is the diffusion coefficient of hydrogen and $C_{k,o}$ is the molar concentration of hydrogen before entering the gas diffusion layer, H_d is the height of the diffusion layer.

2.3. Governing equations for the volume of fluid method

The two-phase volume of fluid (VOF) method used in the present study was developed by Hirt and Nichols [31] for modelling time-dependent flows of multiple immiscible fluids. In the VOF method, the position of the interface of the fluids of interest is tracked via a surface tracking technique on a fixed Eulerian mesh [31]. A volume factor indicator is used to determine the location of the interface and a surface reconstructing technique is used to determine the shape of the interface [32]. Under the VOF method, the surface tension force between the fluids as well as the wall adhesion can be included through a surface force based on the continuum force approach [33].

The governing equations, solved in the present study via the commercial software Fluent 12.1 for the VOF model are given below [32]:

Continuity:

$$\frac{\partial \rho}{\partial t} + \nabla \cdot (\rho \bar{u}) = 0 \quad (28)$$

Momentum:

$$\frac{\partial (\rho \bar{u})}{\partial t} + \nabla \cdot (\rho \bar{u} \bar{u}) = -\nabla P + \nabla \cdot \mu (\nabla \bar{u} + \nabla \bar{u}^T) + \rho \bar{g} + F \quad (29)$$

The surface tension force in Eq. (29) is represented by F . The surface tension force which is expressed as a volume force, is added to the momentum equation as a source term.

To track the interface between phases, a volume fraction continuity equation for one of the phases (water in this case) is solved along with the above equations:

$$\frac{\partial \alpha_q}{\partial t} + \bar{u} \cdot \nabla \alpha_q = 0 \quad (30)$$

where subscript q represents each phase component.

Air volume fraction is obtained from the relation $\sum_{q=1}^2 \alpha_q = 1$.

The properties appearing in the transport equations are determined by the presence of the component phases in each control volume. For example, the density is considered to be:

$$\rho = \sum_{q=1}^2 \alpha_q \rho_q \quad (31)$$

The surface tension effects between the liquid water and air have been considered by using the continuum surface force (CSF) model [33]. According to this model, the volume force is added to the momentum source in Eq. (29) as,

$$F = \sigma \left(\frac{\rho k_1 \nabla \alpha_l}{1} \right) \quad (32)$$

where, σ is the surface tension coefficient, and κ_1 is the surface curvature of the liquid droplet defined in terms of the divergence of the unit normal and is given by,

$$k_1 = \nabla \cdot \bar{n}_1 \quad (33)$$

The unit normal vector, n_1 is calculated from the local gradients in the surface normal at the interface as,

$$\bar{n}_1 = \frac{\nabla \alpha_l}{|\nabla \alpha_l|} \quad (34)$$

Wall adhesion effects are accounted for by adjusting the surface curvature near the wall, where the gas–liquid interface meets the solid wall. The local curvature of this interface is determined by the contact angle, θ_w , which represents the angle between the wall and the tangent to the interface at the wall. The surface normal vector at the wall is given by,

$$\bar{n} = \bar{n}_w \cos \theta_w + \bar{t}_w \sin \theta_w \quad (35)$$

where, \bar{n}_w and \bar{t}_w are the unit vectors normal and tangential to the wall, respectively.

2.4. Solution technique for the Eulerian two-phase mixture model

The numerical methodology involves solving a set of partial differential equations of continuity, momentum, species concentrations involving oxygen, hydrogen, water vapour and liquid water (Eqs. (1), (2) and (4)). This set of equations is supplemented with auxiliary equations to take into account electrochemical reactions. The continuity and momentum equations (Eqs. (1) and (2)) are solved through Ansys Fluent CFD code, while species concentration equations (Eq. (4)) are solved under user defined scalar (UDS) scheme [32]. The convection terms in the governing equations (Eq. (2)) are discretised by the 2nd order upwind scheme and the pressure velocity coupling is achieved by SIMPLE algorithm [32]. The electrochemistry has been treated explicitly with the specification of an average current density of the cell and all relevant parameters are calculated from the auxiliary equations (Eqs. (14)–(27)) after obtaining concentration of species from their respective governing equations (Eq. (4)).

2.4.1. Computational domain and physical parameters

A representative section of a three-dimensional straight channel has been considered in the present study (Fig. 1). The geometry is similar to the computational work of Min [11] and Liu [34]. Physical dimensions of the computational domain as well as the relevant fuel cell parameters are given in Table 1. The computational domain has been meshed with quadrilateral grids of 12,700 cells. A grid sensitivity test using up to 60,000 cells has resulted in similar performance characteristics curve ($V-I$ curve) and it has been concluded that the grid size of 12,700 cells is sufficient to provide grid independency. Simulations have been carried out on a quad core Xeon workstation running on serial server. Each simulation took approximately 2500 iterations to converge in approximately 30–40 min of run time for the case of 0.1–0.6 A cm^{−2} current density, however, it increased to approximately 90 min for 1.0 A cm^{−2} current density. The solution has been considered

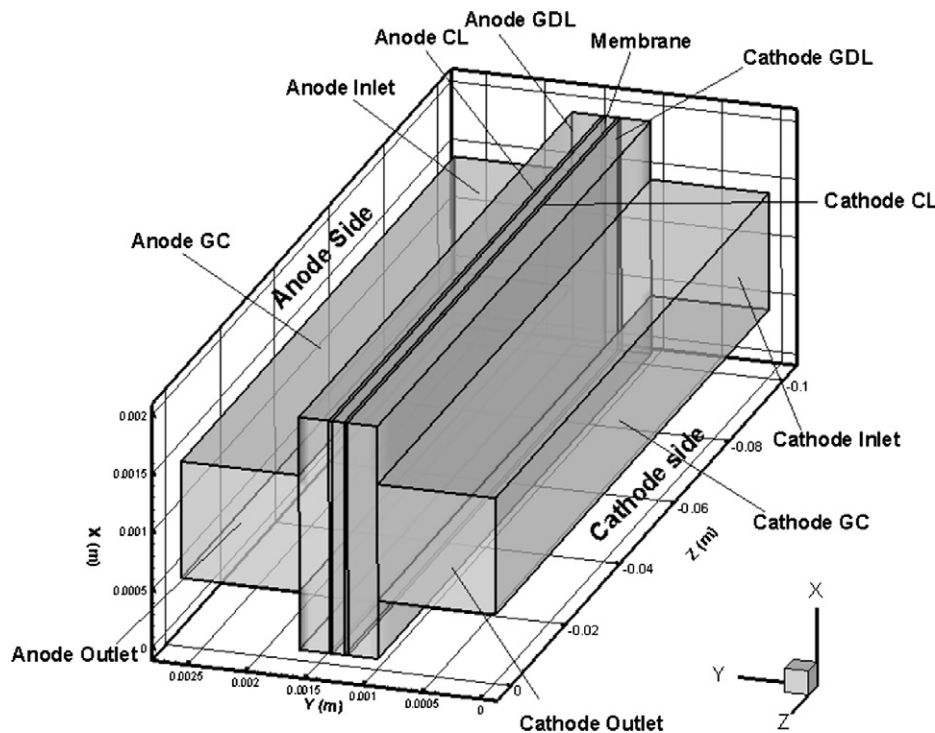


Fig. 1. Schematic diagram of the three-dimensional PEM fuel cell model.

Table 1
Physical parameters and boundary conditions used for the simulations.

Gas channel length $L = 100$ mm	
Gas channel width $W = 1$ mm	[11]
Gas channel height $H_{ch} = 1$ mm	[11]
Diffusion layer height $H_d = 0.254$ mm	[11,34]
Catalyst layer height $H_{ct} = 0.0287$ mm	[11,34]
Land area width $W_l = 1$ mm	[11]
Membrane thickness $t_m = 0.23$ mm	[38]
Permeability $K = 1.76 \times 10^{-11}$ m ²	[11,34]
Faraday constant $F = 96485.309$ C mol ⁻¹	
Operating pressure $P = 101,325$ Pa	
Operating temperature $T = 323$ K	[38]
GDL porosity $\varepsilon_{gdl} = 0.4$	[34]
CL porosity $\varepsilon_{cl} = 0.4$	
Dry mass of membrane $M_{m,dry} = 1.1$ kg mol ⁻¹	
Dry density of membrane $\rho_{m,dry} = 2000$ kg m ⁻³	
Fuel/air stoichiometric ratio $\xi_a/\xi_c = 5/5$	[38]
Electron number of anode reaction $n_a = 4$	
Electron number of cathode reaction $n_c = 2$	
Relative humidity of inlet fuel $RH_a = 100\%$	[38]
Relative humidity of inlet air $RH_c = 0\%$	[38]
Oxygen mass fraction of inlet air $\omega_O = 0.232$	
H ₂ diffusion coefficient at reference state $D_{H_2,ref} = 0.915 \times 10^{-4}$ m ² s ⁻¹	[11]
O ₂ diffusion coefficient at reference state $D_{O_2,ref} = 0.22 \times 10^{-4}$ m ² s ⁻¹	[11]
Water vapour diffusion coefficient at reference state $D_{w,ref} = 0.256 \times 10^{-4}$ m ² s ⁻¹	[11]
Anode exchange current density $i_{a,ref} = 2.0 \times 10^8$ A m ⁻²	[11]
Cathode exchange current density $i_{c,ref} = 160$ A m ⁻²	[11]
Hydrogen reference concentration $C_{H_2,ref} = 56.4$ mol m ⁻³	[11]
Oxygen reference concentration $C_{O_2,ref} = 3.39$ mol m ⁻³	[11]
Anode transfer coefficient $\alpha_a = 0.5$	[11]
Cathode transfer coefficient $\alpha_c = 0.5$	[11]
Water vapour condensation rate $k_c = 1$ s ⁻¹	[11]

converged when the residual of all the governing equations (continuity, momentum and species concentrations) has reached below 1×10^{-6} .

Dirichlet boundary conditions are applied at the cathode and anode inlet. The inlet velocity is a function of stoichiometric flow ratio, ξ_a/ξ_c , geometrical area of membrane A_m and cross-section area of gas channel, A_{ch} , reference current density, I_{ref} and concentration of reactants [11],

$$u_{c, in} = \zeta \frac{I_{ref}}{4F} \frac{1}{x_{O_2, in}} \frac{RT}{P} \frac{A_m}{A_{ch}} \quad (36)$$

$$u_{a, in} = \zeta \frac{I_{ref}}{2F} \frac{1}{x_{H_2, in}} \frac{RT}{P} \frac{A_m}{A_{ch}} \quad (37)$$

At the outlet of the fuel cell, a pressure outlet boundary condition has been applied with a value of zero. A symmetry boundary condition is applied on the side surfaces of the porous regions (Fig. 1). No-slip condition is applied to the external walls.

2.5. Solution technique for the VOF model

The set of governing Eqs. (28)–(30) has been solved in commercial CFD software FLUENT version 12.1. The CFD techniques basically involves discretising of Eqs. (28)–(30) in algebraic form using a control volume method and then solving the set of algebraic equations iteratively. Further details on the computational fluid dynamics technique can be found in Ref. [35]. Getting a converged solution for the two-phase volume of fluid method is very challenging and the accuracy of the solution depends on the interface tracking algorithm [32]. Several optimized algorithms have been selected in the Fluent 12.1 software to aid convergence and to

ensure the accuracy of the volume of fluid model. These algorithms include the pressure–velocity coupling through the PISO scheme and the interface tracking between gas–liquid through geo-reconstruct scheme [32]. The PISO scheme involves solving the continuity and momentum equations iteratively (Eqs. (28) and (29)) with solving an additional pressure correction step [36]. Though the PISO scheme takes more computational time per solver steps, it significantly reduces the total number of iterations required for the convergence [32]. In geometric reconstruct scheme, the interface between the air and water is determined by a piecewise linear interface calculation method [32]. It is based on the assumption that the interface between each phase inside a computational cell can be approximated by a straight line with an appropriate inclination and the slope of the interface line can be calculated based on the calculated volume fraction and its derivative at each cell. Once the interface is reconstructed, the fluid volume passing between adjacent cells in the computational domain can be calculated from the discretised form of Eq. (30). Further details on the geometric reconstruction can be found in Ref. [37].

2.5.1. Computational domain and boundary condition for the VOF model

In the present study, a cathode channel of a PEM fuel cell has been represented by a $250 \mu\text{m} \times 250 \mu\text{m} \times 1000 \mu\text{m}$ section as shown in Fig. 2. This computational domain is similar to the study of Zhu et al. [19] and Ding et al. [21]. The bottom wall is the GDL surface and is treated as a solid rather than a porous wall. The GDL surface is specified as hydrophobic with a static contact angle of 140° , whereas the side and top walls are treated as hydrophilic with a static contact angle of 45° . This combination of surface wettability has provided the best water removal through the cathode channel in previous studies [19,21]. Two different water inlet diameters of $50 \mu\text{m}$ and $20 \mu\text{m}$ have been used in the present study and the distances among the water pores have been varied by $200 \mu\text{m}$, $150 \mu\text{m}$, $100 \mu\text{m}$ and $75 \mu\text{m}$.

The computational domain has been meshed with 442,566 hexahedral cells. A minimum mesh size of $5.5 \mu\text{m}$ has been used to mesh the domain. Instead of carrying out a grid independency test, the grid independency has been insured by comparing grids with similar reported studies. For a similar geometry, Ding et al. [21] used a minimum mesh size of $10 \mu\text{m}$ and obtained a grid independent solution with 82,625 hexahedral cells. Zhu et al. [19] used 62,835 hexahedral cells for a similar geometry. Therefore, it is expected that the use of 442,566 hexahedral cells would be enough to provide grid independent results in the present study. Inlet air velocity has been set at 10 m s^{-1} . In many previous studies an air velocity of 10 m s^{-1} has been used [16,19,21]. In contrary, different values of water velocity have been used for similar studies. Zhu et al. [19] have used a value of 1 m s^{-1} for the base case and have provided a parametric study of inlet water velocity varying from 0.05 m s^{-1} to 2 m s^{-1} . They have shown that the effects of water velocity become negligible for water velocity below 1 m s^{-1} . Ding

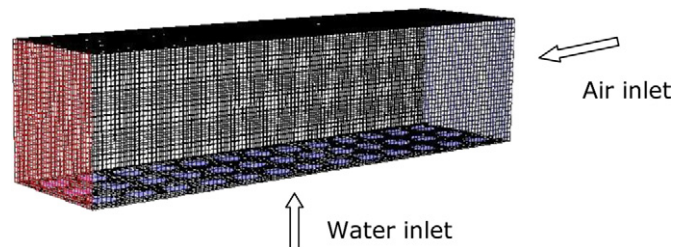


Fig. 2. Three-dimensional computational domain with mesh representing cathode channel.

et al. [21] on the other hand used a value of 0.0625 m s^{-1} . The water generation rate can be calculated using the electrochemical reaction formula $S = (I + 2\alpha/2F)M_{\text{H}_2\text{O}}$. At 1.0 A cm^{-2} , the net water transfer coefficient has been obtained to be 0.85 in the present study using the Eulerian two-phase model. Therefore, the water generation rate has been calculated to be $2.518 \times 10^{-4} \text{ g s}^{-1} \text{ cm}^{-2}$, which yields a velocity of $2.49 \times 10^{-4} \text{ m s}^{-1}$ through the $50 \mu\text{m}$ diameter pores with the assumption that all the produced water has been condensed to liquid water. The present simulation results using the Eulerian two-phase mixture model also gives an average velocity in the order of 10^{-4} m s^{-1} in the catalyst layer/GDL layer (discussed in Section 3.1). The water generation rate and therefore the water injection velocity would also be influenced by the relative humidity of the air and hydrogen streams as well as modelling parameters used. However, specifying such a small water injection velocity in the volume of fluid model would require a large computational time for the water to accumulate in the channel. Ding et al. [21] have shown that due to the large difference in air and water velocity, a several order of magnitude increases in water velocity would not fundamentally change the water dynamics, but would expedite the computation. In the present study, therefore, the water injection velocity has been set at 0.0625 m s^{-1} for the base case following the work of Ding et al. [21]. The time step used in the calculation was $1\text{e}^{-6} \text{ s}$.

3. Results and discussion

3.1. Simulated results from the Eulerian two-phase mixture modelling

3.1.1. Performance characteristics

A common practice in developing computational fuel cell model is to verify the simulated results of V – I performance characteristics curve against experimental data. Fig. 3 shows the computed V – I characteristics curve and experimental data from Ticianelli et al. [38]. The V – I characteristic curves presented in Fig. 3 show that the computational model provides a very good agreement with the experimental data up to a current density of 0.8 A cm^{-2} . At higher current density, the present model overpredicts the voltage. The experimental data of Ticianelli et al. [38] has been widely used as a kind of benchmark for validating numerical modelling [34,39]. However, the exact geometry of the fuel cell used in the experiment of Ticianelli [38] is unknown. The operating pressure, temperature and the Nafion 117 membrane used in the Ticianelli et al.'s experiment [38] have been utilised in the present study. Where the relevant parameters are not known from the Ticianelli et al.'s

experiment [38], these have been taken from previous reported modelling studies [11,34,39] and are given in Table 1. There are many other reasons for the discrepancy in the simulated result at higher current densities including uncertainty in using explicit electrochemistry model, the value of constant in the condensation rate equation, and the kinetic parameters used such as the exchange current density and the charge coefficients. Another important factor that may influence the accuracy of the simulation is the assumption of isothermal condition. In actual operation of fuel cells, due to electrochemical reaction, heat is generated at the catalyst layer, which leads to a temperature gradient across the GDL from the catalyst layer to the channel. The simulation results by Berning et al. [39] and Min [40] show that the temperature at the catalyst layer on the cathode side is approximately 3°C higher than that in the flow channel. This non-uniform temperature distribution would not only influence nearly all the fuel cell empirical properties, but also would influence water saturation in the GDL. Therefore, further improvement in the accuracy of the prediction could be made by including a heat transfer model in future work.

3.1.2. Velocity field

The velocity vectors along the length in the gas channels are shown in Fig. 4(a) at a current density of 1 A cm^{-2} . The flow takes on a parabolic profile due to the assumption of wall no-slip conditions and becomes fully developed on both the sides of the PEM fuel cell. However, it is important to note that the GDL channel interface does not enforce a no-slip boundary condition since the interface is porous. However, the interface imposes significantly reduced rate of transport resulting in the parabolic velocity profile in the channel. The velocity in the cathode channel is significantly higher than that in the anode channel to meet the stoichiometric balance of the reactants required to maintain the electrochemical reaction at the catalyst. In GDL and CL, much slower velocity magnitude was observed.

Fig. 4(b) shows the vector plot at the mid-plane of the assembly. In this plot vector lengths are kept constant as the velocity varies widely among different zones. The high speed gas channel flow affects the GDL flow field considerably. The velocity direction in the cathode GDL is mainly longitudinal caused by the high convective velocity in the flow channel. In the anode channel, the velocity vectors become lateral to the main flow directions, especially at the downstream.

In GDL and CL, much slower velocity magnitude was observed. This suggests the transport limitations of fresh reactants through the porous regions. The transport of reactants through the porous zones is one of the critical parameters as it determines the reaction rates, thus, defines the overall power output of the cell. Unfortunately, there is no experimental data available in the literature to verify the velocity fields. The results presented here are qualitatively very similar to the velocity fields presented in Dawes et al.'s [41] numerical study. It is important to note that Dawes et al. [41] used slightly different fuel cell geometry and operating conditions.

3.1.3. Species concentrations

Fig. 5 shows the contour plots of mass fraction of oxygen, water vapour and liquid water in the cathode side at a current density of 1.0 A cm^{-2} . Oxygen diffuses from the cathode channel through the gas diffusion layer towards the catalyst layer, where the oxygen is consumed. The diffusion of oxygen through the GDL and into the land area is shown by curved contours. The mass fraction of oxygen under the land area at downstream locations is small, where the mass transport limitations are more prominent. The mass fraction of oxygen drops along the flow channel as oxygen is consumed and also due to the increased volume fraction of water. It should be noted that the detailed description of reactions distribution inside

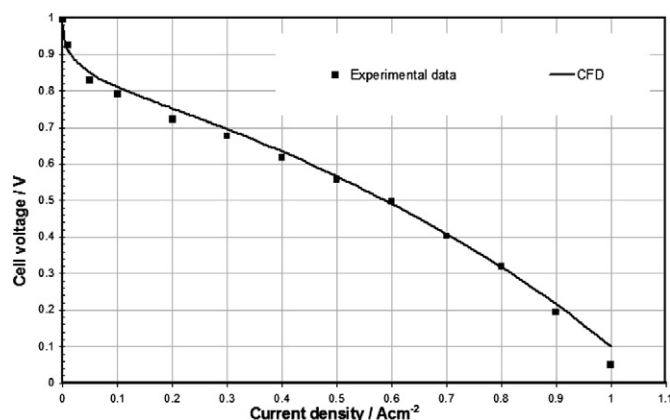


Fig. 3. Comparison of simulated results with measurement for predicting V – I characteristics curve.

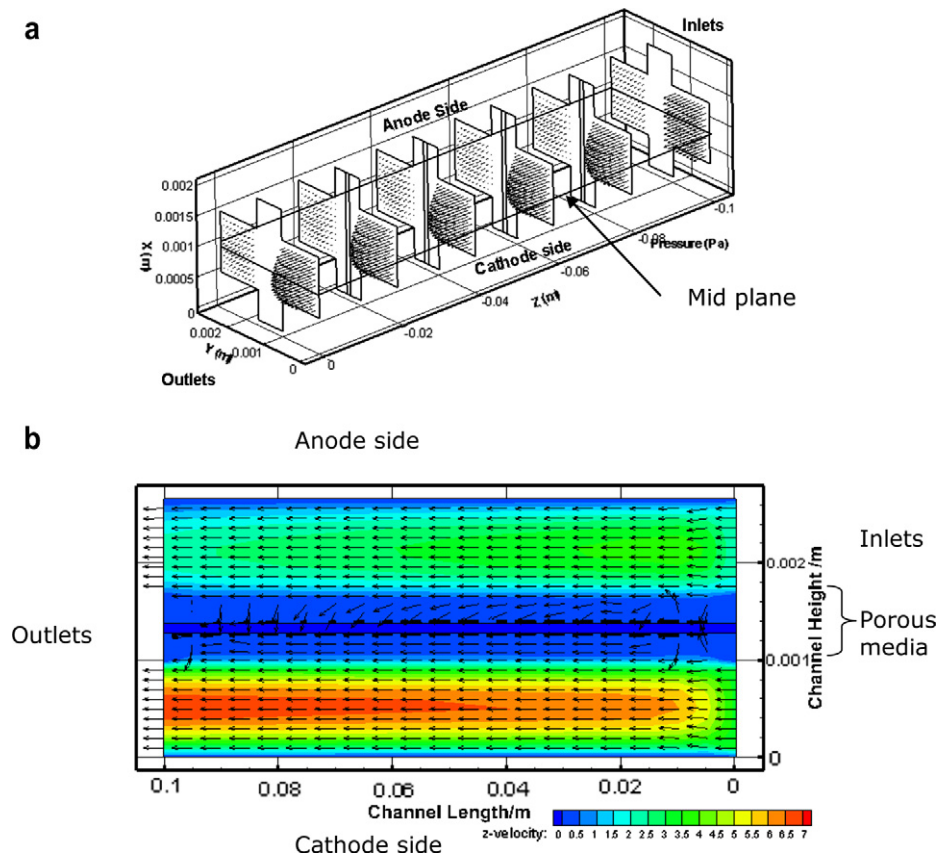


Fig. 4. (a) Velocity vectors along the length of the model. (b) Velocity vector along the length at the mid-plane of the fuel cell at the current density of 1 A cm^{-2} . The arrows show the direction and the colour shows the magnitude of the velocity.

a PEM fuel cell measured in situ has not been reported in the literature. However, the oxygen distribution presented here is very similar to the reported modelling study of Berning et al. [39] and Dawes et al. [41]. It is observed from the figure that the water vapour mass fraction increases along the channel due to water produced by electrochemical reaction and water coming from the anode side to the cathode side by electro-osmotic process. Again, more water vapour is produced under the land area because of the low velocity of air under the land allows more humidification of dry air. This water vapour then condenses to produce liquid water. The figure shows that the liquid water is mostly trapped under the land area. Therefore, special attention is necessary to manage water trapped under the land area.

The simulation results show that a large amount of liquid water is trapped under the land area, whereas the amount of liquid water in the channel is very small. The Eulerian two-phase modelling only provides overall average values and this technique cannot predict the dynamic behavior of the emergence of liquid water as droplet, and subsequent droplet growth, coalescing and slug or water film formation in the channel. Therefore, a VOF based interface tracking model, which is capable of providing information regarding the dynamic behavior of water flow has been implemented and the simulation results have been presented in Section 3.2. The results from the Eulerian model, however, highlight that the area under the land is critical for water management and effective design or operating parameter should be found to remove this trapped liquid.

3.2. Simulated results from the VOF multi-phase modelling

Due to electrochemical reaction in a PEM fuel cell taking place at $60\text{--}80^\circ\text{C}$, the produced water often condenses in the GDL and is

then transported through the GDL pore network into the flow channel. Due to the complex nature of GDL pore network it is very difficult to simulate the water transport through the pore network into the channel. In the present study, the water emergence into the channel has been studied with various locations of water pore distribution on the GDL–channel interface. This approach is similar to the work of Ding et al. [21,22]. Fig. 6 shows a schematic drawing of the arrangement of the pores on the gas diffusion layer surface. In the figure L_1 is the inter-pore distance in the longitudinal direction, L_2 is the distance from the wall to the pore in the lateral direction and L_3 is the inter-pore distance in the lateral direction. Table 2 gives the various combinations of water inlet diameter and inter-pore spaces that have been used in the present study.

3.2.1. Water dynamics for the base case

In the base case simulation, $50 \mu\text{m}$ diameter pores have been distributed on the GDL surface at $75 \mu\text{m}$ interval in both longitudinal and lateral directions. Fig. 7 shows the water flow pattern inside the cathode channel. From the figure, three stages of water transport can be observed: (i) emerging and merging of droplets, (ii) formation of slug, and (iii) accumulation of slugs on the side and top walls and detachment from the top wall.

In the initial phase, water droplets emerge from the pores, merge with each other and then form slugs. Slugs are pushed downward by air pressure as shown at 1.75 ms . At 2.5 ms , the two slugs merge into a larger body and at 3.25 ms , the front of the slug leaves the channel. At the same time, the back of the slug body touches the side walls and due to hydrophilicity of the wall, the water body spreads as a film on the wall. The water film gets wider and thicker with the passage of time due to continuous inpouring of water from the pores. Eventually the water film on the side wall

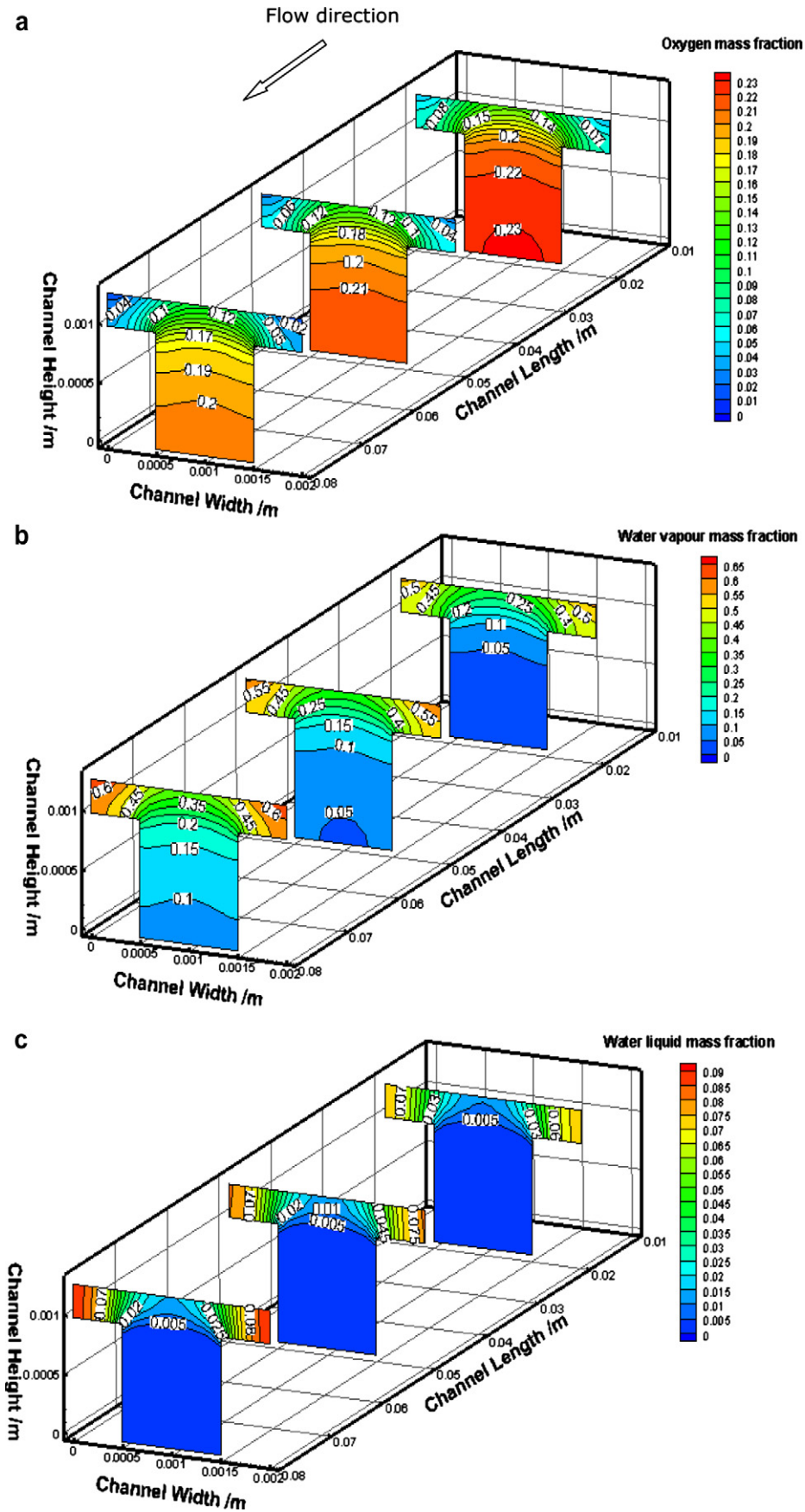


Fig. 5. Contour plots of mass fraction of (a) oxygen, (b) water vapour and (c) liquid water at the cathode side.

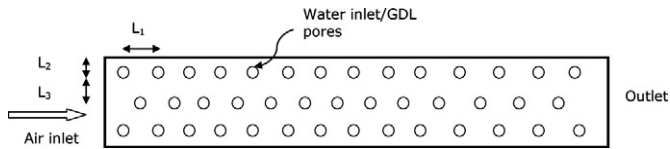


Fig. 6. A schematic drawing of the pore arrangement on the gas diffusion layer surface.

Table 2

Simulation cases for different locations of water emergence as describe in Fig. 6.

Case number	Water inlet diameter, μm	Inter-pore distances
1 (base case)	50	75 μm in both directions, 3 rows ($L_1 = 75 \mu\text{m}$, $L_2 = 50 \mu\text{m}$, $L_3 = 75 \mu\text{m}$)
2	50	150 μm in longitudinal direction, 75 μm in lateral direction, 3 rows ($L_1 = 150 \mu\text{m}$, $L_2 = 50 \mu\text{m}$, $L_3 = 75 \mu\text{m}$)
3	50	75 μm , two columns, distance from walls 62.5 μm ($L_1 = 75 \mu\text{m}$, $L_2 = 62.5 \mu\text{m}$, $L_3 = 75 \mu\text{m}$)
4	50	100 μm , two columns, distance from walls 62.5 μm ($L_1 = 100 \mu\text{m}$, $L_2 = 62.5 \mu\text{m}$, $L_3 = 75 \mu\text{m}$)
5	50	150 μm , two columns, distance from walls 62.5 μm ($L_1 = 150 \mu\text{m}$, $L_2 = 62.5 \mu\text{m}$, $L_3 = 75 \mu\text{m}$)
6	50	200 μm , two columns, distance from walls 62.5 μm ($L_1 = 200 \mu\text{m}$, $L_2 = 62.5 \mu\text{m}$, $L_3 = 75 \mu\text{m}$)
7	20	200 μm , two columns, distance from walls 62.5 μm ($L_1 = 200 \mu\text{m}$, $L_2 = 50 \mu\text{m}$, $L_3 = 75 \mu\text{m}$)

reaches the top wall (4 ms) and then detach from the main body along the top wall (5 ms). At the same time, a second water film starts to grow on the side wall. This water film is pushed along the side wall (8 ms) and eventually flushed out of the channel. The whole cycle then repeats itself at an interval of 10 ms with the formation of slug similar to at 1.75 ms. It is worth noting that though the growth and detachment of slugs are non-linear cyclic process, the water emergence and mergence are continuous. Another observation from the simulation is that the hydrophilicity of the side and top walls play a key role in water removal. The hydrophilic side and top walls allow water to form film, to spread out and then to be driven out from the channel quickly.

The importance of side and top walls on water transport is clearly observed from the simulation results presented in this section. The key finding from this section is that the hydrophilic wall allows the liquid water to spread as film and removes water quickly from the GDL surface. Though the present study uses a different pore structure, the present study corroborates the benefit of hydrophilic side walls for water removal as presented by Ding et al. [21,22].

3.2.2. Effects of water inlet structures

It is clear from the base case simulation that a large proportion of the GDL surface is covered with liquid water, which would prevent fresh oxygen to diffuse through the surface and thus reducing the fuel cell performance. In order to optimize water dynamics in the channel, further simulations have been carried out with different inlet pore structures.

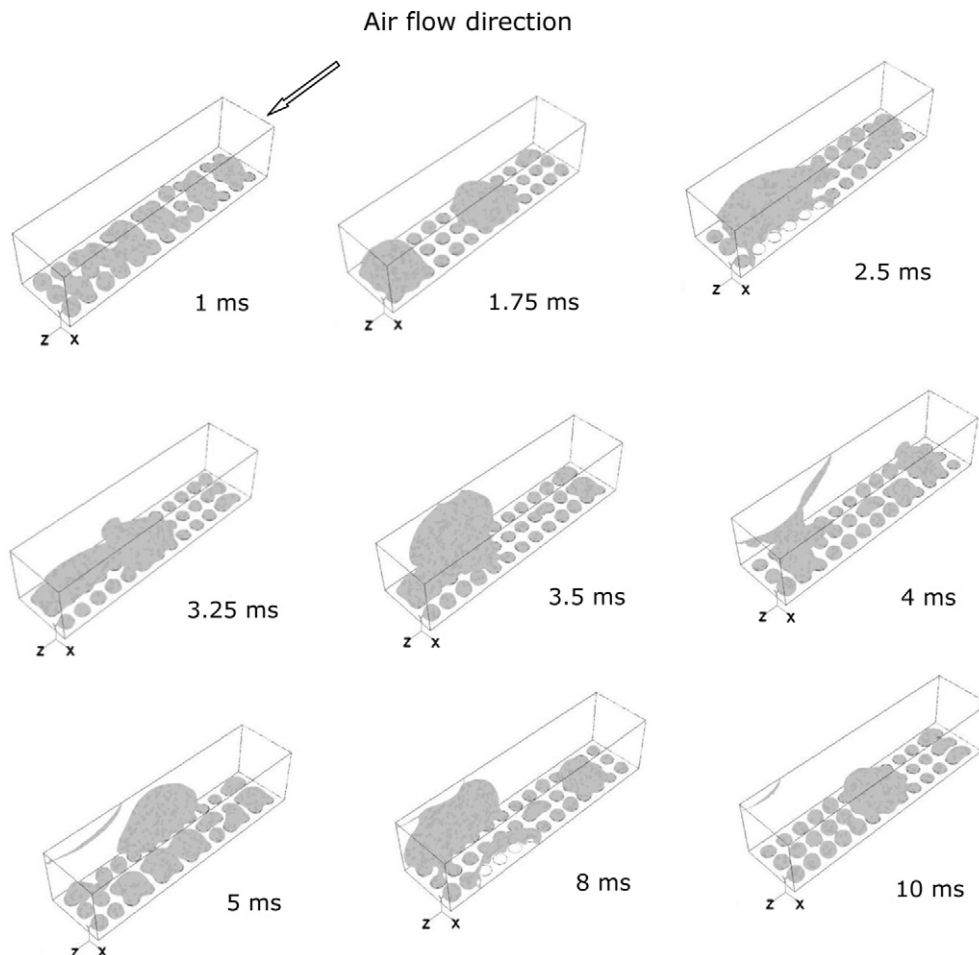


Fig. 7. Water flow pattern inside the cathode for the base case.

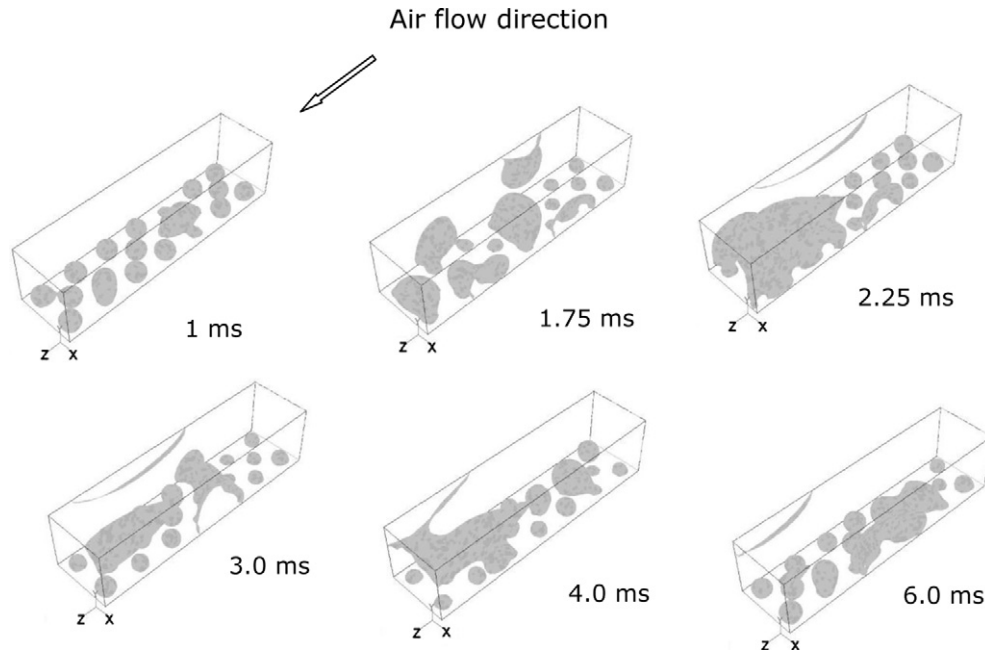


Fig. 8. Water flow pattern inside the cathode for case 2.

Fig. 8 shows the two-phase flow pattern for the case 2, where water pores staggered with the longitudinal distance between the two consecutive pores is $150\ \mu\text{m}$. Because of the higher inter-pore distances, the droplets after emerging from the pores, get more spaces to grow in larger sizes as seen in Fig. 7 at 1 ms. At this stage, the droplets are nearly spherical due to the hydrophobic nature of the GDL surface. At 1.75 ms, the droplets coalesce with each other and form a large number of smaller blobs of water on the GDL surface as well as on the side and top walls. At 2.25 ms, these individual blobs of water flows further downstream and form a large slug on the GDL surface and a thin film on the top wall. At 3.0 ms, the slug body is almost flushed out from the channel by the

air pressure. At 4.0 ms, the water film at the top wall re-merges with the slug, blocking the air flow. At 6.0 ms, the slug is flushed out and at the same time, smaller blob of water body starts to form again. With this pore arrangement, the simulation results show that there is less surface coverage of the GDL by water and this would make more surface area of GDL available for oxygen diffusion. However, still a large portion of the GDL surface is covered by water slug and further optimization of the pore arrangement is required to reduce the surface coverage of the GDL.

In order to take advantage of water removal characteristics of the hydrophilic side walls, further simulations have been carried out with water pores arranged in two columns at a distance of

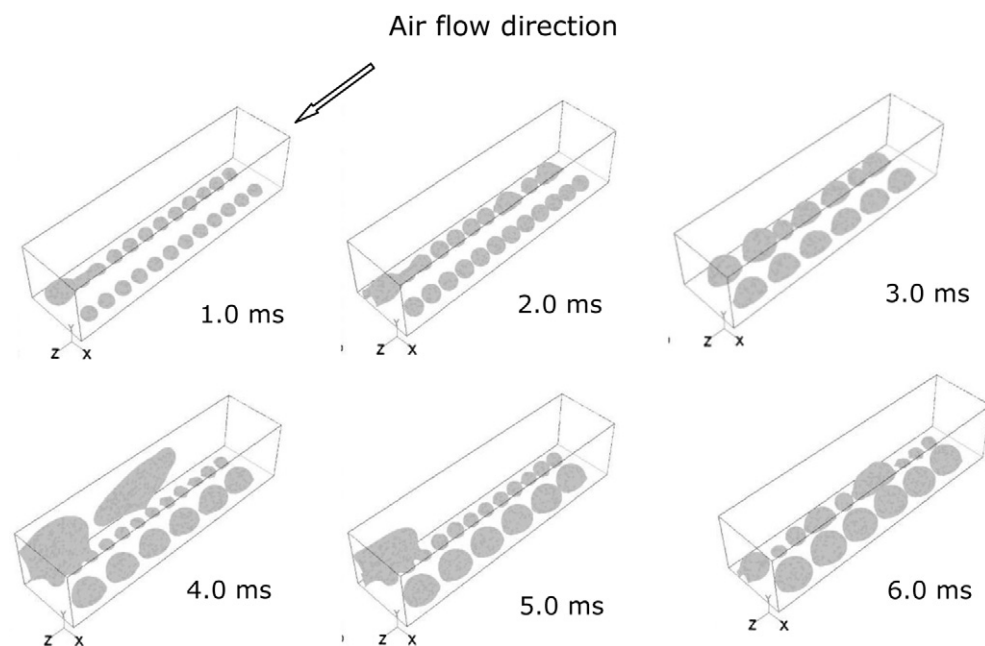


Fig. 9. Water flow pattern for $50\ \mu\text{m}$ pore and $75\ \mu\text{m}$ inter-pore distance, case 3.

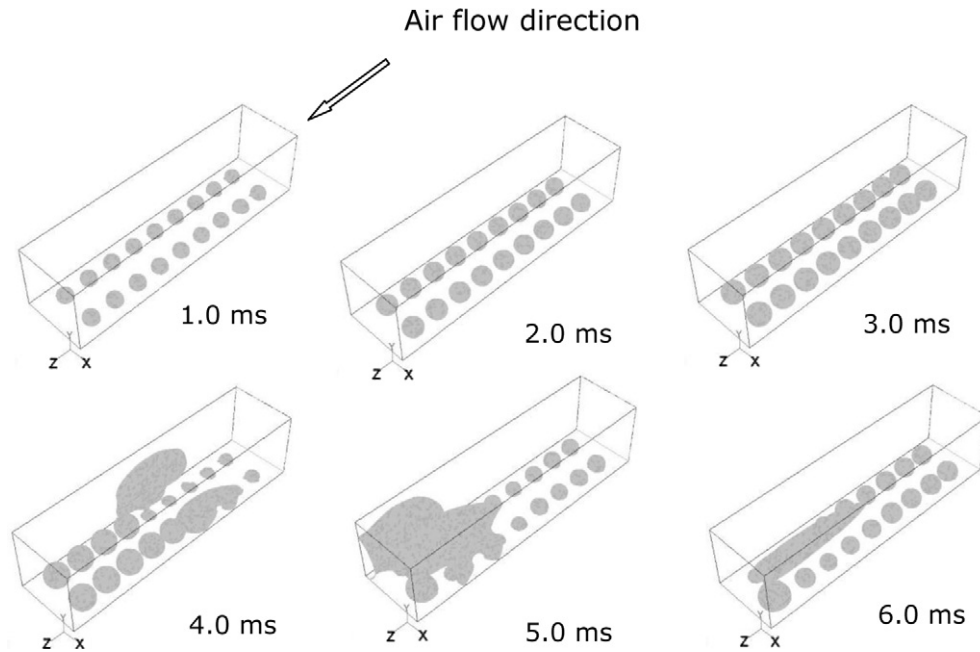


Fig. 10. Water flow pattern for 50 μm pore and 100 μm inter-pore distance, case 4.

62.5 μm from the side walls and with different longitudinal inter-pore distances. Figs. 9–12 show the water flow patterns for inter-pore spaces of 75 μm , 100 μm , 150 μm and 200 μm respectively. The qualitative water flow patterns in these four cases are quite similar. In every case, the droplets emerge from the pores and grow in sizes while retaining their spherical shape due to the hydrophobicity of the GDL surface. Droplets then coalesce with each other forming a slug. The slug then touches the side wall and because of the hydrophilicity of the side wall, spreads quickly in

the form of a water film. The water film on the side wall eventually reaches the top wall and is then driven out of the channel. It is observed from Figs. 9–12 that the higher the inter-pore distances, the lower the surface coverage of the GDL.

It is clear from the simulation results that the water inlet structures have significant effects on the liquid water transport through the channel and controlling the water inlet structures on the GDL surface could be one of the methods for optimising water management.

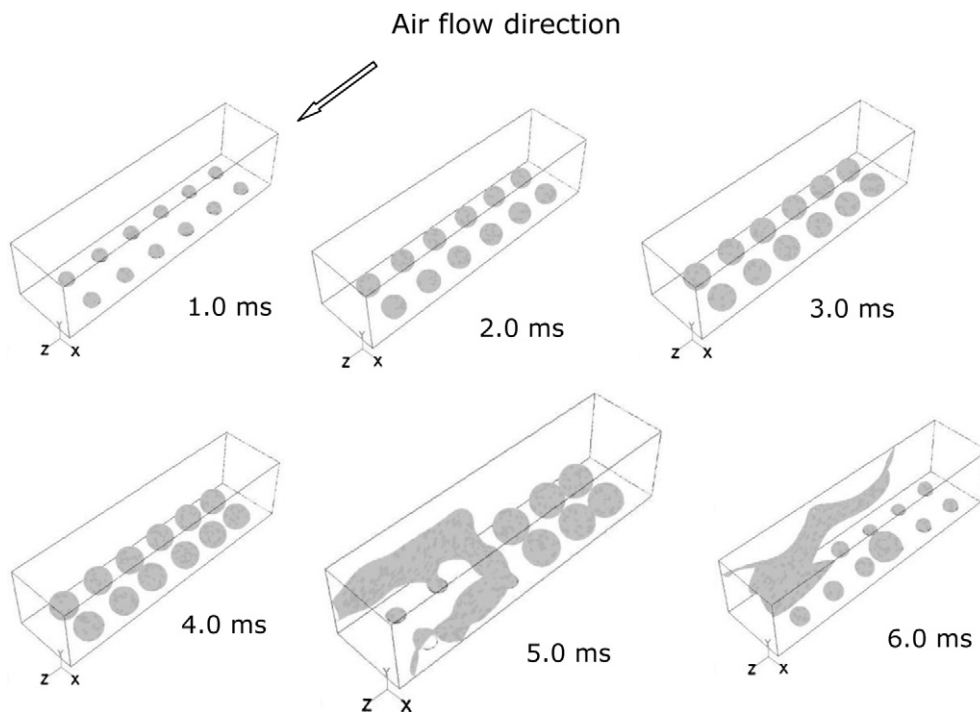


Fig. 11. Water flow pattern for 50 μm pore and 150 μm inter-pore distance, case 5.

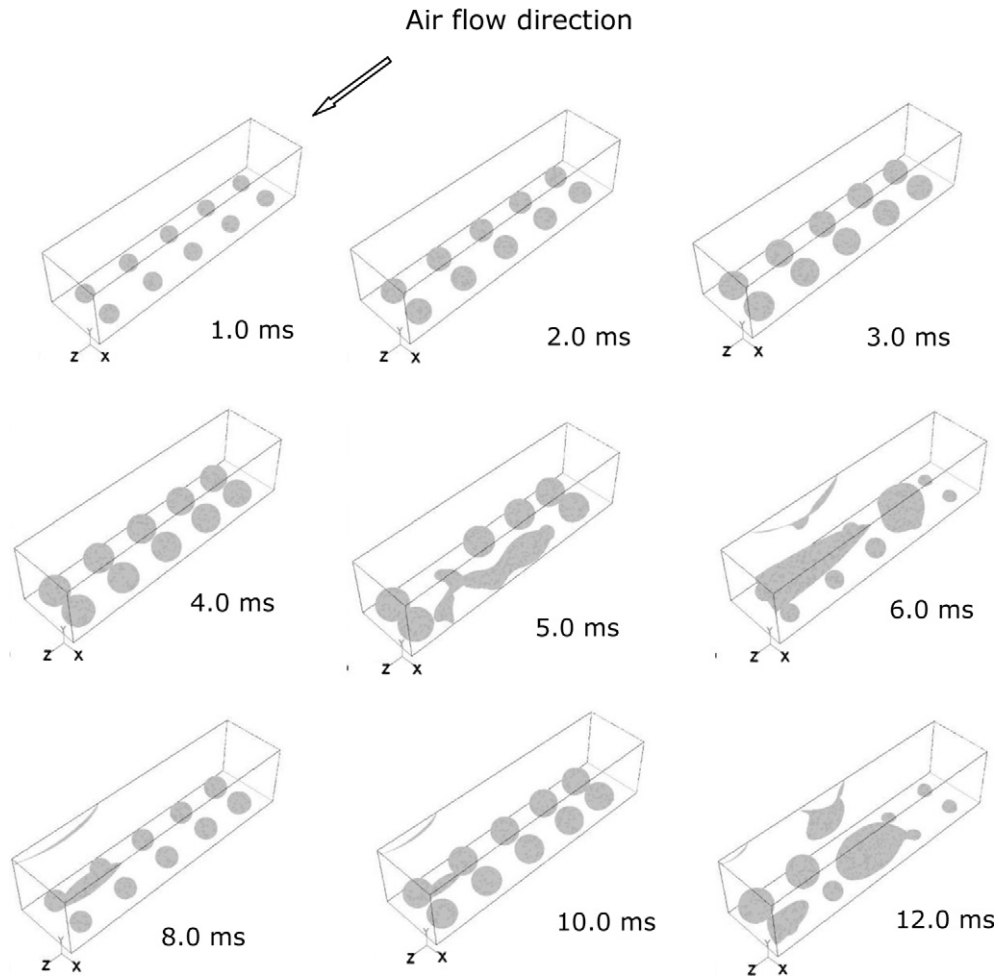


Fig. 12. Water dynamics for 50 μm pore and 200 μm inter-pore distance, case 6.

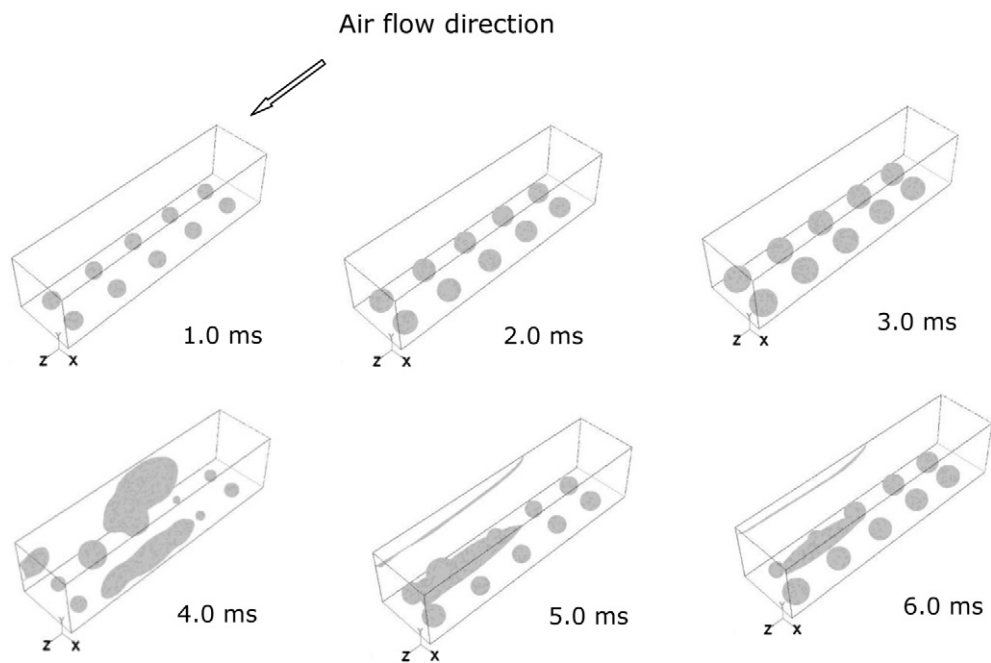


Fig. 13. Water flow pattern for 20 μm pore and 200 μm distance, case 7.

3.2.3. Effects of pore diameter

Fig. 13 shows the dynamic water behavior for the case where the pore diameter of is $20\ \mu\text{m}$ and the inter-pore space is $200\ \mu\text{m}$. Compared to $50\ \mu\text{m}$ diameter pore, the simulation results show that the smaller pore diameter leads to an early detachment of droplets from the pores. With smaller pore diameter, there is less connectivity of the water droplet with the pore resulting in a smaller surface tension force. Therefore the shear and pressure force on the droplets overcome the surface tension force early and the size of droplet at detachment is smaller compared to those droplets emerging from larger pores. The smaller droplet size at detachment has also been observed by Zhu et al. [19]. Further details on the forces acting on a single droplet and the effects of droplet aspect ratio, channel dimension and air velocity can be found in Refs. [42–44]. Early detachment of droplets leads to a lesser interaction of droplets with each other and which results in lower surface coverage of GDL with water. This is evident by comparing Figs. 6 and 12. As shown in Fig. 6 at $4.0\ \text{ms}$, the droplet is still growing when emerging from $50\ \mu\text{m}$ pores, while at $4.0\ \text{ms}$, the droplets emerging from $20\ \mu\text{m}$ pores are already sheared off and interacted with other droplets as shown in Fig. 12.

3.2.4. Time evolution of flow pattern

Fig. 14 shows the pressure drop, surface and volume coverage ratio for the base case, alternative blocked-off inlets (case 2) and an optimized GDL arrangement of $50\ \mu\text{m}$ diameter with $200\ \mu\text{m}$ inter-pore distances (case 6). The pressure drop across the channel represents the parasitic loss related to the pumping of air, the surface coverage ratio indicates the fraction of GDL surface covered by water compared to the total surface area, while the volume coverage ratio indicates the fraction of volume occupied by water compared to the volume of the channel. In order to make a PEM fuel cell more efficient, the pressure drop and the surface and volume coverage should be minimised.

For the base case, the pressure drop, surface and volume coverage ratio increase steadily up to $2\ \text{ms}$ indicating the droplets emergence, growth and merger with each other. After $2\ \text{ms}$, the surface coverage ratio drops rapidly, which coincides with the water slugs touching the sidewalls and spreading as a water film. When water drops resides on the GDL surface, they occupy more cross-sectional area of the channel. As a result, the pressure drop is high. Once the droplets touch the side walls, and spread as a film, the water occupies less cross-sectional area and the pressure loss decreases. After $2\ \text{ms}$, the pressure drop, the surface and volume coverage ratio starts to fluctuate indicating a very non-linear process. There appears to be a correlation between the pressure drop and volume coverage ratio. The surface coverage ratio does not seem to correlate with the pressure drop.

For case 2, where inter-pore distances are larger compared to the base case, the droplets can grow larger, without much interaction with each other. As a result, the surface coverage ratio is lower compared to the base case. The pressure variation in this case is highlighted by the two peaks at approximately $3.5\ \text{ms}$ and $8\ \text{ms}$. Interestingly the pressure drop does not seem to correspond to the surface coverage ratio, rather it corresponds to the size of the slugs located on the GDL surface i.e. the cross-sectional area of channel occupied by the water (see Fig. 7 at $4.0\ \text{ms}$). For the case 2, the volume coverage ratio is very similar to the base case; however, the surface coverage ratio is smaller, which is an indication that this arrangement of pores would allow more oxygen to reach the reaction sites.

For the case 6, where the water pores are arranged near the side walls with inter-pore distances of $200\ \mu\text{m}$, the surface and volume coverage are smaller compared to the other cases. Moreover, a distinctive cyclic variation in the pressure drop and the surface

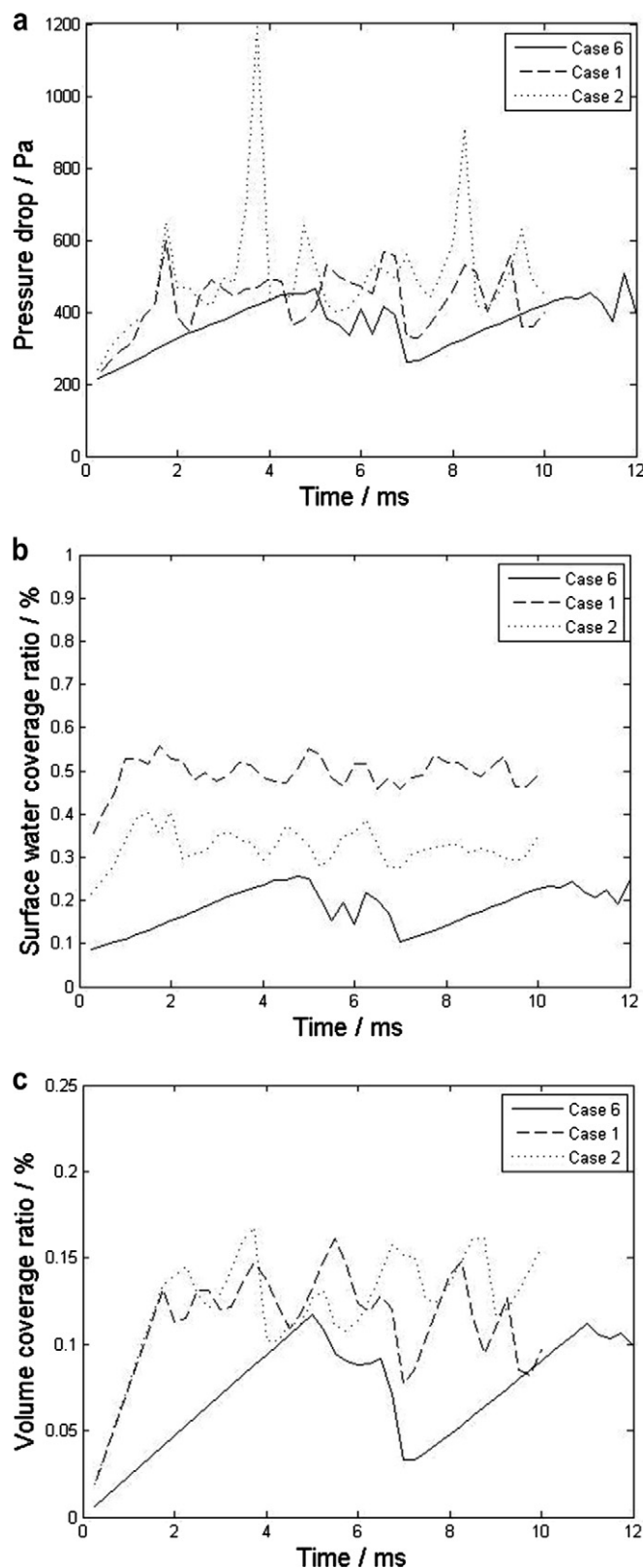


Fig. 14. Time variation of (a) pressure (b) surface coverage and (c) volume fraction for the base case, case 2 and case 6.

and volume coverage ratio have been observed. In this case, the water droplets emerge, grow, deflect, and merge into larger slugs and since the pores are arranged near the side walls, the slugs quickly touch the side walls. Aided by the hydrophilicity of the side

walls, the slugs spread thinly as a film on the side walls before reaching the top wall. The water film is then flushed away from the channel quicker along the walls. This case produces the smallest surface coverage and pressure drop and should lead to an improved fuel cell performance.

Fig. 15 shows the variation of surface coverage ratio for different pore sizes. The 20 μm diameter pore produces a slightly lower surface coverage ratio compared to the 50 μm diameter. With the increase of inter-pore distance, the surface coverage ratio decreases and this effect is more pronounced for the 50 μm diameter water pores.

3.3. Discussion on the GDL design for better water removal

The results presented above show that the surface coverage ratio of a GDL can be reduced by having water pores arranged near the side walls. However, in the conventional GDL design, the water path into the channel cannot be controlled due to the random distribution of fibres inside a GDL structure. There are several mechanisms for transporting water from the catalyst layer through the GDL towards the flow channels. Several studies have investigated the water drainage in the GDL under purging condition and have identified that at higher saturation level the liquid water is transported in a capillary flow and at lower saturation level in a phase change induced flow [45–47]. Lu et al. [25] have also investigated the water transport in a GDL in ex-situ experiment and concluded that liquid water transport takes place through preferential paths and the water breakthrough into the channel is intermittent. The water breakthrough takes place only at few sites. However, an in-situ experiment of an operating fuel cell has shown that the water breakthrough takes place at many GDL sites [25]. The increase of the number of water breakthrough sites in an operating fuel cell may have been caused by the vapour phase water transport [25]. Due to the temperature gradient across the GDL, the water vapour transported from the CL to the channel condenses inside the GDL forming micro-droplets. These micro-droplets then condense to form macro-droplets, which then follow preferentially through larger pores and then breakout into the channel [25]. This mechanism was proposed by Nam and Kaviani as “inverted tree-like water transport” [48]. It is quite clear from the discussion above that the water transport through a GDL is very complex and it is not very clear which path the liquid water takes inside a GDL and

breakouts into the cathode channel. However, some studies have shown how the water path through a GDL can be controlled. A simulation study of liquid water transport within a reconstructed GDL layer made of selective introduction of hydrophilic passages within the GDL shows that the liquid water invades into the GDL selectively through the hydrophilic path [49]. A pore network modelling study by Sinha and Wang [50] also shows that a controlled wettability distribution of hydrophobic and hydrophilic paths allows liquid water to flow preferentially through the connected hydrophilic paths. It is evident that incorporating a mixed wettability GDL layer would lead to the precise control of water path through the GDL into the channel near the channel walls and the present study shows that this would significantly improve transport of water through the flow channel.

4. Conclusion

The present study focuses on the investigation of water dynamics inside a polymer electrolyte membrane fuel cell using two different modelling approaches: the Eulerian two-phase mixture and the volume of fluid interface tracking models. The Eulerian multi-phase model has provided overall information of species distribution inside a fuel cell and identified that liquid water usually accumulates under the land area. Further, the liquid water transport through a cathode channel of a PEM fuel cell has been thoroughly investigated employing an interface tracking volume of fluid (VOF) model in order to develop a fuel cell design for better water management. The simulation results show that the water transport can be broadly described as: emergence of droplets, interaction with neighboring droplets, formation of slug, movement of slug along the channel and the walls and eventual flushing out. The whole process is highly non-linear. The present study shows that the water transport in the channel could be optimized by controlling the arrangement of water pore in the GDL surface. In particular, by reducing the pore diameter, by placing water inlets near the channel walls and by increasing the inter-pore distance; the surface coverage of the GDL by water can be greatly reduced. A GDL layer made of a column of hydrophilic fiber arranged inside the randomly distributed hydrophobic fibre matrix could provide a controlled and predictable path of water into the channel and that would lead to a better water management in the channel.

Nomenclature

a_k	water activity
A	specific area of the catalyst layer (m^{-1})
C	molar concentration (mol m^{-3})
d	pore diameter (m)
D	diffusion coefficient ($\text{m}^2 \text{s}^{-1}$)
E	equilibrium thermodynamic potential (V)
F	Faraday constant ($96485.309 \text{ C mol}^{-1}$)
F	surface tension force (N m^{-3})
g	acceleration due to gravity (m s^{-2})
H	height (m)
i	reaction rate (A m^{-3})
I	average current density (A m^{-2})
K	permeability (m^2)
k_c	condensation rate (s^{-1})
k_m	phase conductivity of membrane (S m^{-1})
L	length (m)
M	molar mass (kg mol^{-1})
$M_{m,dry}$	dry mass of membrane (kg mol^{-1})
n	electron number for reactions
n_d	electro-osmotic drag coefficient
P	pressure (Pa)

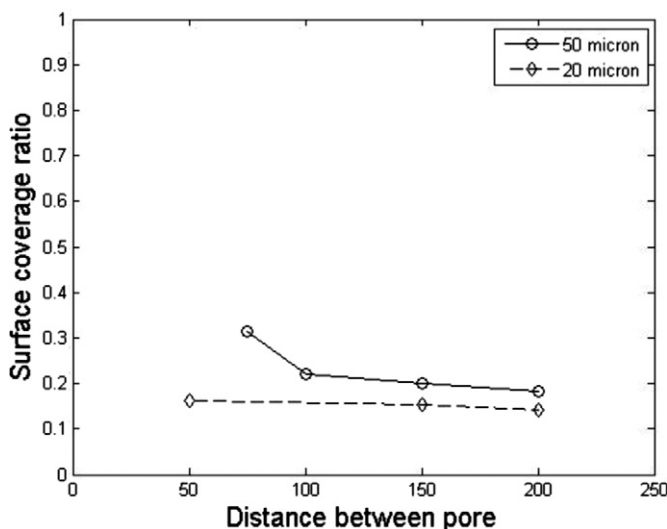


Fig. 15. The profile of surface coverage ratio for different inter-pore distances and pore diameters.

R	gas constant ($8.314 \text{ J mol}^{-1} \text{ K}^{-1}$)
RH	relative humidity
S	source term
s	liquid water saturation
t	time (s)
t_m	membrane thickness
T	temperature (K)
\mathbf{u}	velocity vector (m s^{-1})
V_{cell}	cell voltage (V)
W	width (m)
X	molar fraction
x,y,z	co-ordinate

Greek symbols

α	net water transfer coefficient
α	volume fraction
ε	porosity
η	overpotential (V)
θ	contact angle
μ	viscosity ($\text{kg m}^{-1} \text{ s}^{-1}$)
ζ	stoichiometric ratio
ρ	density (kg m^{-3})
σ	surface tension force (N m^{-1})
ω	mass fraction

Subscripts and superscripts

0	before diffusion layer
a	anode
act	activation
av	average
c	cathode
$conc$	concentration
d	diffusion layer
eff	effective
el	electron
H_2	hydrogen
k	species
L	limiting
m	membrane
O_2	oxygen
ohm	ohmic polarization
pro	proton
q	phases
ref	reference
sat	saturation
wv	water vapour
w	wall

Abbreviation

CL	catalyst layer
GDL	gas diffusion layer
PEM	polymer electrolyte membrane
VOF	volume of fluid

References

- [1] Sandstede G, Cairns EJ, Bagotsky VS, Wiesener K. History of low temperature fuel cells. In: Vielstich W, Gasteiger HA, Lamm A, Yokokawa H, editors. Handbook of fuel cells – fundamentals, technology and applications. John Wiley and Sons; 2010.
- [2] Yoon W, Weber AZ. Modeling low-platinum-loading effects in fuel-cell catalyst layers. J Electrochem Soc 2011;158:B1007–18.
- [3] Ohma A, Mashio T, Sato K, Iden H, Ono Y, Sakai K, et al. Analysis of proton exchange membrane fuel cell catalyst layers for reduction of platinum loading at Nissan. Electrochim Acta 2011;56:10832–41.
- [4] Spornjak D, Prasad AK, Advani SG. Experimental investigation of liquid water formation and transport in a transparent single-serpentine PEM fuel cell. J Power Sources 2007;170(2):334–44.
- [5] Natarajan D, Nguyen TV. Three-dimensional effects of liquid water flooding in the cathode of a PEM fuel cell. J Power Sources 2003;115:66–80.
- [6] Wang ZH, Wang CY, Chen KS. Two-phase flow and transport in the air cathode of PEM fuel cells. J Power Sources 2001;94:40–50.
- [7] You L, Liu HT. A two-phase flow and transport model for the air cathode in PEM fuel cells. Int J Heat Mass Transfer 2002;45:2277–87.
- [8] You L, Liu H. A two-phase flow and transport model for PEM fuel cells. J Power Sources 2006;155:219–30.
- [9] Berning T, Djilali N. A 3D, multiphase, multicomponent model of the cathode and anode of a PEM fuel cell. J Electrochem Soc 2003;150:A1589–98.
- [10] Mazumder S, Cole JV, Rigorous 3-D mathematical modelling of PEM fuel cells, II. Model predictions with liquid water transport. J Electrochem Soc 2003;150(11):A1510–7.
- [11] Min CH. Performance of a proton exchange membrane fuel cell with stepped flow field design. J Power Sources 2009;186:370–6.
- [12] Meng H. A three dimensional mixed-domain PEM fuel cell model with fully-coupled transport phenomenon. J Power Sources 2007;164:688–96.
- [13] Khan MA, Sundén B, Yuan J. Analysis of multi-phase transport phenomena with catalyst reactions in polymer electrolyte membrane fuel cells – a review. J Power Sources 2011;196:7899–916.
- [14] Cai YH, Hu J, Ma HP, Yi BL, Zhang HM. Effects of hydrophilic/hydrophobic properties on the water behavior in the micro-channels of a proton exchange membrane fuel cell. J Power Sources 2006;161(2):843–8.
- [15] Zhan Z, Xiao J, Pan M, Yuan R. Characteristics of droplet and film water motion in the flow channels of polymer electrolyte membrane fuel cells. J Power Sources 2006;160(1):1–9.
- [16] Jiao K, Zhou B. Innovative gas diffusion layers and their water removal characteristics in PEM fuel cell cathode. J Power Sources 2007;169:296–314.
- [17] Quan P, Zhou B, Sobiesiak A, Liu Z. Water behaviour in serpentine micro-channel for proton exchange membrane fuel cell cathode. J Power Sources 2005;152:131–45.
- [18] Zhu X, Sui PC, Djilali N. Dynamic behaviour of liquid water emerging from a GDL pore into a PEMFC gas flow channel. J Power Sources 2007;172:287–95.
- [19] Zhu X, Sui PC, Djilali N. Three-dimensional numerical simulations of water droplet dynamics in a PEMFC gas channel. J Power Sources 2008;181:101–15.
- [20] Zhu X, Liao Q, Sui PC, Djilali N. Numerical investigation of water droplet dynamics in a low-temperature fuel cell microchannel: effect of channel geometry. J Power Sources 2010;195:801–12.
- [21] Ding Y, Bi HT, Wilkinson DP. Three-dimensional numerical simulation of water droplet emerging from a gas diffusion layer surface in micro-channel. J Power Sources 2010;195:7278–88.
- [22] Ding Y, Bi HT, Wilkinson DP. Three dimensional numerical simulation of gas-liquid two-phase flow patterns in a polymer-electrolyte membrane fuel cells gas channel. J Power Sources 2011;196:6284–92.
- [23] Ous T, Arcoumanis C. Visualisation of water droplets during the operation of PEM fuel cells. J Power Sources 2007;173:137–48.
- [24] Ous T, Arcoumanis C. Visualisation of water accumulation in the flow channels of PEMFC under various operating conditions. J Power Sources 2009;187:182–9.
- [25] Lu Z, Daino MM, Rath C, Kandlikar SG. Water management studies in PEM fuel cells, part III: dynamic breakthrough and intermittent drainage characteristics from GDLs with and without MPLs. Int J Hydrogen Energy 2010;35(9):4222–33.
- [26] Bazylak A, Sinton D, Djilali N. Dynamic water transport and droplet emergence in PEMFC gas diffusion layers. J Power Sources 2008;176(1):240–6.
- [27] Yu LJ, Ren GP, Qin MJ, Jing XM. Transport mechanisms and performance simulations of a PEM fuel cell with interdigitated flow field. Renew Energy 2009;34:530–43.
- [28] Nam J, Kaviany M. Effective diffusivity and water-saturation distribution in single- and two-layer PEMFC diffusion medium. Int J Heat Mass Transfer 2003;46(24):4595–611.
- [29] Springer TE, Zawodzinski TA, Gottesfeld S. Polymer electrolyte fuel cell model. J Electrochem Soc 1991;138(8):2334–42.
- [30] Lum KW, McGuirk JJ. Three-dimensional model of a complete polymer electrolyte membrane fuel cell-model formulation, validation and parametric studies. J Power Sources 2005;143:103–24.
- [31] Hirt CW, Nichols BD. Volume of fluid (VOF) method for the dynamics of free boundaries. J Comput Phys 1981;39(1):201–25.
- [32] Fluent user's guide. Fluent Inc.; 2011.
- [33] Brackbill JU, Kothe DB, Zemach C. A continuum method for modeling surface tension. J Comput Phys 1992;100:335–54.
- [34] Liu X, Tao W, Li Z, He Y. Three-dimensional transport model of PEM fuel cell with straight flow channels. J Power Sources 2006;158:25–35.
- [35] Versteeg HK, Malalasekera W. An introduction to computational fluid dynamics: the Finite volume method. 2nd ed. England: Pearson, Prentice Hall, Harlow; 2007.
- [36] Issa RI. Solution of the implicit discretised fluid flow equations by operator splitting. J Comput Phys 1986;62:40–65.
- [37] Youngs DL. Time-dependent multi-material flow with large fluid distortion. In: Morton KW, Baines MJ, editors. Numerical methods for fluid dynamics. New York: Academic Press; 1982.
- [38] Ticianelli EA, Derouin CR, Srinivasan S. Localization of platinum in low catalyst loading electrodes to attain high power densities in SPE fuel cells. J Electroanal Chem 1998;251:275–95.

- [39] Berning T, Lu DM, Djilali N. Three-dimensional computational analysis of transport phenomena in a PEM fuel cell. *J Power Sources* 2002;106:284–94.
- [40] Min C-H. A novel three-dimensional, two-phase and non-isothermal numerical model for proton exchange membrane fuel cell. *J Power Sources* 2010;195(7):1880–7.
- [41] Dawes JE, Hanspal NS, Famioly OA, Turan A. Three-dimensional CFD modeling of PEM fuel cells: an investigation into the effects of water flooding. *Chem Eng Sci* 2008;64:2781–94.
- [42] Kumbur EC, Sharp KV, Mench MM. Liquid droplet behavior and instability in a polymer electrolyte fuel cell channel. *J Power Sources* 2006;161:333–45.
- [43] Cho SC, Wang Y, Chen KS. Droplet dynamics in a polymer electrolyte fuel cell gas flow channel: forces, deformation, and detachment. I: theoretical and numerical analyses. *J Power Sources* 2012;206:119–28.
- [44] Cho SC, Wang Y, Chen KS. Droplet dynamics in a polymer electrolyte fuel cell gas flow channel: forces, deformation, and detachment. I: comparisons of analytical solution with numerical and experimental results. *J Power Sources* 2012;210:191–7.
- [45] Turhan A, Heller K, Brenizer JS, Mench MM. Passive control of liquid water storage and distribution in a PEFC through flow-field design. *J Power Sources* 2008;180(2):773–83.
- [46] Khandelwal M, Mench MM. An integrated modeling approach for temperature driven water transport in a polymer electrolyte fuel cell stack after shutdown. *J Power Sources* 2010;195(19):6549–58.
- [47] Cho KT, Mench MM. Coupled effects of flow field geometry and diffusion media material structure on evaporative water removal from polymer electrolyte fuel cells. *Int J Hydrogen Energy* 2010;35(22):12329–40.
- [48] Nam JH, Kaviany M. Effective diffusivity and water saturation distribution in single- and two layer PEMFC diffusion medium. *Int J Heat Mass Transfer* 2003;46:4595–611.
- [49] Hao L, Cheng P. Lattice Boltzmann simulations of water transport in gas diffusion layer of a polymer electrolyte membrane fuel cell. *J Power Sources* 2010;195:3870–81.
- [50] Sinha PK, Wang C-Y. Liquid water transport in a mixed gas diffusion layer of a polymer electrolyte fuel cell. *Chem Eng Sci* 2008;63:1081–91.